

Enhancing the Photoactivity of Faceted BiVO₄ via Annealing in Oxygen-Deficient Condition

Hui Ling Tan, Adrian Suyanto, Alexandra T. De Denko, Wibawa H. Saputera, Rose Amal,* Frank E. Osterloh, and Yun Hau Ng*

Thermal annealing of metal oxides in oxygen-deficient atmosphere, particularly reducing hydrogen gas, has been demonstrated to induce oxygen vacancy formation for enhanced photoactivity of the materials. Here, it is demonstrated that argon annealing (another prevalently used oxygen-deficient gas) in the temperature range of 300–700 °C greatly affects the activity of dual-faceted BiVO₄ microcrystals for photocatalytic O₂ generation and photocurrent generation. While treatment at 300 °C has little to no effect, higher temperatures of 500 and 700 °C significantly improve the crystallinity, alter the local structure distortion, and reduce the bandgap energy of the treated BiVO₄. The higher temperature treatment also favors formation of new subgap states attributed to oxygen vacancies, as supported by surface photovoltage and electron paramagnetic resonance spectroscopies. Despite the most profound improvements in structural, optical, and electronic properties displayed by the 700 °C-treated BiVO₄, the sample annealed at 500 °C exhibits the highest photoactivity. The lower activity of the 700 °C-treated BiVO₄ is ascribed to the creation of bismuth vacancies and the loss of well-defined crystal facets, contributing to impeded electron transport and poor charge separation.

size and shape.^[1b,c,3] Alteration of these physicochemical properties affects the charge generation and the kinetic behaviors (including charge separation and transport) of the photoinduced electron–hole pairs, rendering thermal annealing a promising method to improve the activity of various photocatalysts.

In addition to the above-mentioned variation in properties, more recent studies on thermal annealing revealed that the environment in which the treatment occurs has an impact on the defect states of the treated metal oxides.^[4] Generally, annealing atmospheres can be classified into two categories: oxygen-rich and oxygen-deficient. The typical examples of the former are oxygen (O₂) and air atmospheres, whereas the latter includes nitrogen (N₂), hydrogen (H₂), and argon (Ar) gases. Annealing of metal oxide in oxygen-rich atmosphere was demonstrated to behave differently from that in oxygen-deficient atmosphere: oxygen-rich

suppresses oxygen vacancy formation, while oxygen-deficient favors it. Mtangi et al.^[4b] showed that subjection of ZnO to H₂ and Ar annealing introduced a new defect (possibly oxygen vacancy), which on the other hand was absent after O₂ treatment. Likewise, Yamada et al.^[5] suggested that the oxygen vacancies in nitrogen-doped TiO₂ were increased via N₂ treatment, but decreased after air treatment. While oxygen vacancies are the most prevalent surface structural defects of an oxide material, they are known as the shallow donors for metal oxide photocatalysts.^[6] Augmentation of oxygen vacancies is therefore beneficial for improving donor densities and facilitating charge transport to enhance the photoactivity of metal oxide materials. Formation of oxygen vacancies has also been claimed to introduce subgap states to extend the light absorption ability of various metal oxides.^[7]

H₂ annealing or hydrogenation has been utilized as a general strategy to introduce oxygen vacancies in several metal oxides such as α -Fe₂O₃, ZnO, TiO₂, and WO₃, resulting in significantly enhanced photoelectrochemical (PEC) performance.^[6] Despite being simple and effective, extra care has to be exercised during its experimental setup as H₂ gas is hazardous. The strong reducing ability of H₂ may also result in undesirable reduction effects. For example, hydrogenation of TiO₂/FTO (fluorine-doped tin oxide) photoelectrode at high temperatures (>450 °C) was reported to cause damage to the FTO conducting layer due

1. Introduction

Earlier studies on thermal annealing have manifested the treatment as a facile route to tailor the grain size, phase composition, and morphology of metal oxide photocatalysts. Provision of thermal energy promotes crystal grain growth for improved crystallinity, thus reducing the number of recombination centers to result in better charge separation.^[1] The temperature dependence of phase transformation processes also allows such heat treatment to facilitate the formation of the more thermodynamically stable photocatalyst.^[2] Furthermore, the lowering of surface free energy in response to heat treatment can also instigate morphological changes in terms of particle

H. L. Tan, A. Suyanto, W. H. Saputera,
Prof. R. Amal, Dr. Y. H. Ng
Particles and Catalysis Research Group
School of Chemical Engineering
The University of New South Wales
Sydney, NSW 2052, Australia
E-mail: r.amal@unsw.edu.au; yh.ng@unsw.edu.au

A. T. D. Denko, Prof. F. E. Osterloh
Department of Chemistry
University of California
Davis, CA 95616, USA

DOI: 10.1002/ppsc.201600290



to SnO₂ reduction to Sn metal.^[8] This thus restricts the hydrogenation temperature, which then limits the extent of improvement attainable for the physicochemical properties of a material. Considering these issues, annealing treatment in alternative oxygen-deficient conditions (e.g., N₂ and Ar gases) can be a safer option for controlled generation of oxygen vacancies in metal oxides.

As a visible-light-responsive photocatalyst, monoclinic BiVO₄ with a 2.4–2.5 eV bandgap and deep valence band energy level has attracted much research attention due its strong oxidizing ability. In the presence of a sacrificial electron acceptor, BiVO₄ is highly active for water oxidation under visible light and is therefore a prominent oxygen-evolving photocatalyst for water splitting.^[9] However, the photoactivity of BiVO₄ is restricted by quick charge recombination and poor electron transport. Li et al.^[10] discovered faceted BiVO₄ with exposed {010} and {110} surfaces is capable of assisting charge separation, owing to the difference in energy levels of different facets. However, such crystal facet engineering approach does not modify the optical and electronic properties of BiVO₄ that can fundamentally enhance its photoactivity.^[11] On the contrary, annealing in oxygen-deficient atmospheres such as H₂^[7c,12] and N₂^[7b] was shown to be effective in reducing the bandgap and increasing the donor density of BiVO₄ via introduction of oxygen vacancies as well as hydrogen impurities in the former and N-doping in the latter. These variations in properties were demonstrated to improve photon absorption and charge transportation for enhanced PEC performance of BiVO₄.

To the best of our knowledge, there is yet any studies investigating the influences of annealing treatment in oxygen-deficient conditions (particularly Ar treatment) on the physicochemical and electronic properties of faceted BiVO₄. Better understanding of the effects can help to further optimize the photoactivity of faceted BiVO₄, which has been demonstrated to possess better charge separation. In this work, Ar treatment is elucidated to substantially affect water oxidation activities (both powder suspension (PS) and PEC systems) of dual-faceted BiVO₄, which is highly dependent on the annealing temperature in the range of 300–700 °C. This is attributed to the variation in crystallinity, local structure distortion, optical and electronic properties, and morphology of the BiVO₄ upon heat treatment.

2. Results and Discussion

Dual-faceted BiVO₄ with dominating oxidation functional {110} facets was synthesized using the method reported in our recent work^[11] and annealed under Ar atmosphere at different temperatures, namely, 300, 500, and 700 °C. Herein, the treated BiVO₄ samples are denoted as Ar T , where T represents the annealing temperature. The effect of Ar treatment on the photoactivity of BiVO₄ was determined using the water oxidation reaction via two approaches: PS and PEC method. In the PS system, BiVO₄ powder was suspended in an aqueous silver nitrate (AgNO₃)

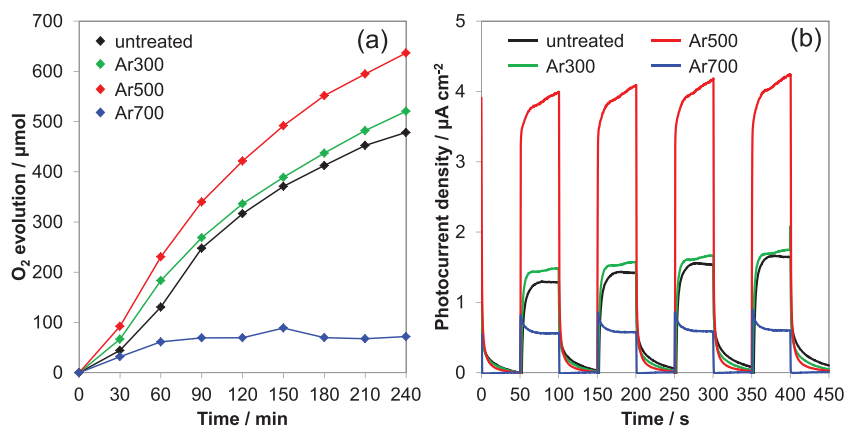


Figure 1. a) Photocatalytic O₂ evolution and b) PEC photocurrent generation from BiVO₄ samples annealed at 300, 500, and 700 °C under Ar atmosphere in comparison to the as-synthesized (untreated) sample.

solution in which the O₂ gas evolved during visible light ($\lambda > 420$ nm) illumination was monitored. Evidently, Ar treatment affects the photocatalytic water oxidation activity of BiVO₄, as depicted in **Figure 1a**. While annealing at a moderately low temperature of 300 °C barely altered the water oxidation photoactivity of BiVO₄ as compared to the as-synthesized (untreated) BiVO₄, the water oxidation rate was greatly improved for the BiVO₄ annealed at 500 °C, but considerably impaired when the annealing temperature was further increased to 700 °C. In contrast to other samples that showed ongoing O₂ gas evolution throughout 4 h illumination, the amount of O₂ gas generated by Ar700 sample plateaued after 1 h of illumination.

For the PEC system, the BiVO₄ powder samples were made into electrodes via dropcast method using FTO as the substrates. Upon light irradiation on the BiVO₄ photoanode, concurrent with hole-mediated water oxidation reaction on the surface of the photoanode, electrons are drawn off as current through the external circuit to the counter electrode. Comparison of the photocurrent magnitude is thus another technique to evaluate the BiVO₄'s photoactivity in response to the annealing treatment under Ar environment at different temperatures. The PEC performance of BiVO₄ has been demonstrated to be restricted by its poor electron transport properties.^[13] This limiting factor can be overcome by illuminating the BiVO₄/FTO electrode from the FTO side (backside illumination) such that electron–hole pairs are generated closer to the electron collector (FTO substrate), minimizing the travel distance of electrons. **Figure 1b** compares the anodic photocurrent densities of the untreated BiVO₄ with the Ar-treated samples, measured at an applied potential of 0 V versus Ag/AgCl at pH 6 under visible light ($\lambda > 420$ nm) irradiation from the backside. Interestingly, the BiVO₄ samples exhibit similar behavior in PEC photocurrent generation with that of PS water oxidation activity trend, that is Ar700 < untreated \approx Ar300 < Ar500.

To understand the interplay between Ar annealing treatment and the physical and optical properties of BiVO₄, X-ray diffraction (XRD), Raman, and UV–vis diffuse reflectance were carried out for each BiVO₄ sample, as delineated below. XRD patterns in **Figure 2a** show that the single-phase scheelite-monoclinic structure of the as-synthesized BiVO₄ was preserved

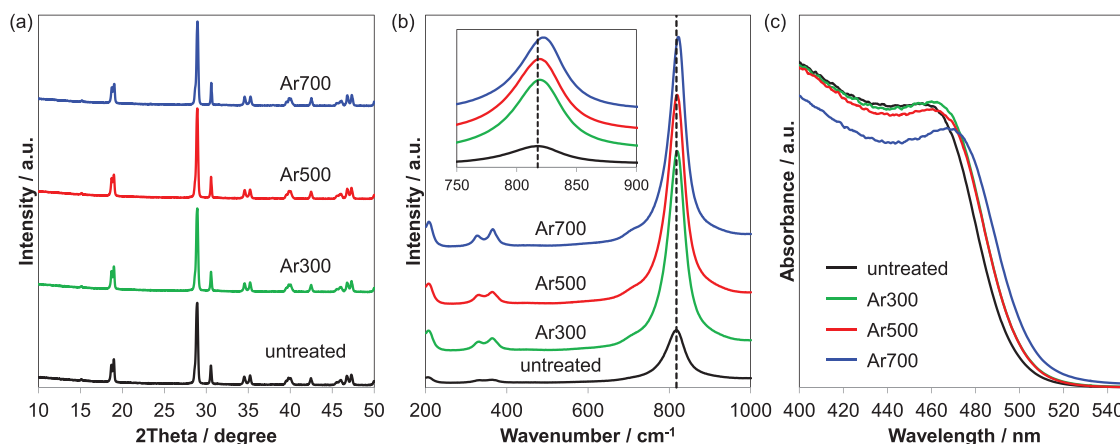


Figure 2. a) XRD diffraction peaks, b) Raman, and c) UV-vis spectra of BiVO_4 before and after Ar annealing treatment at 300, 500, and 700 °C.

after Ar annealing treatment at different temperatures in the range of 300–700 °C. Crystallite size (Table 1) estimation using the Scherrer equation indicates the BiVO_4 crystals enlarge with the increase of annealing temperature, particularly for those with relatively higher temperatures of 500 and 700 °C. Such increase of crystallite size, indicative of improved crystallinity, has been commonly reported for thermal treatment of oxide semiconductors, be it in air or oxygen-deficient ambient.^[1a,14] The enhanced crystallinity ensuing from Ar treatment is supported by the substantially narrower Raman peaks of the Ar-treated BiVO_4 samples compared to the untreated BiVO_4 ,^[12,15] as displayed in Figure 2b. In fact, the peak width gradually decreases as the annealing temperature increases.

The Raman spectra of all samples exhibit the characteristic vibrational bands of BiVO_4 .^[16] Specifically, the 324 and 366 cm^{-1} bands are related to the deformation modes of VO_4^{3-} tetrahedron, whereas the bands at 710 and 818 cm^{-1} correspond to the respective asymmetric and symmetric stretching modes of V–O bond.^[15,17] Raman spectroscopy has been demonstrated as a useful technique that is sensitive to the variation in the local structure of BiVO_4 .^[18] For this, Raman analysis was performed and confirmed using more than one arbitrarily chosen location on each of the BiVO_4 powder samples. Enlarged view of the dominant 818 cm^{-1} band (inset in Figure 2b) shows that it is shifted to higher frequencies with greater annealing temperatures, suggesting the decrease of V–O bond length according to the empirical correlation between Raman stretching frequencies and V–O bond lengths.^[19] The position of the dominant Raman band and the corresponding V–O bond length for each

Table 1. Effects of Ar annealing treatment on the crystallite size, local structure, and bandgap energy of BiVO_4 .

Sample	Crystallite size [nm]	Raman band [cm^{-1}]	V–O bond length ^{a)} [Å]	Bandgap [eV]
Untreated	81	818	1.701	2.49
Ar300	85	819	1.700	2.47
Ar500	112	819	1.700	2.47
Ar700	272	823	1.698	2.44

^{a)} $\nu[\text{cm}^{-1}] = 21\,349 \exp(-1.9176R[\text{Å}])$.^[19]

sample are listed in Table 1. Owing to the Bi^{3+} electron lone-pair-induced distortion of the VO_4^{3-} tetrahedron in monoclinic BiVO_4 , shorter V–O bond length infers greater lone-pair distortion around the Bi^{3+} cation, thus leading to greater overlap between the Bi 6p and O 2p orbitals at the valence band. Such greater orbital overlap has been reported to prompt enhanced photogenerated hole migration to the surface of BiVO_4 to conduct water oxidation reaction.^[18a]

The variation in BiVO_4 's local structure distortion (i.e., degree of orbital overlap) by Ar annealing treatment is reinforced by the change in its optical properties as reflected in the UV-vis diffuse reflectance spectra (Figure 2c). Although all samples display optical absorption in the visible light region, the absorption edges of the Ar-treated samples are red-shifted with respect to that of the untreated BiVO_4 , as most significantly evinced by Ar700. Bandgap energy estimation from the absorption edges indicates the bandgap of BiVO_4 decreases as the annealing temperature increases (Table 1).

In order to probe the photochemical charge separation in as-synthesized and Ar-annealed BiVO_4 samples, surface photovoltage spectroscopy (SPS) measurements were conducted on thin films of the particles on a gold substrate. SPS sensitively measures photochemical charge transport and detects interfacial trap sites^[20] and defect states.^[21] This is achieved by following the light-induced change in the contact potential difference (ΔCPD vs gold (Au) reference) of the BiVO_4 films as a function of the illumination energy, using a Kelvin probe. Measurements were conducted in vacuum after wetting the films with a drop of methanol. Methanol acts as a sacrificial electron donor and improves the photovoltage signal from BiVO_4 by reacting with the photoholes.^[22]

The SPS spectrum of the untreated BiVO_4 is shown in Figure 3a. A negative ΔCPD signal develops at photon energies near the optical bandgap of the material and reaches a local maximum of -0.12 V at 3.0 eV. The spectrum resembles those previously measured for BiVO_4 nanoparticles.^[23] Similarly, the photovoltage signal in Figure 3a can be attributed to the injection of photoelectrons from BiVO_4 into the Au substrate as shown in the energy diagram in Figure 3c. Based on the difference between the work function of the Au substrate (5.3 eV) and the conduction band edge of BiVO_4 (4.76 eV),

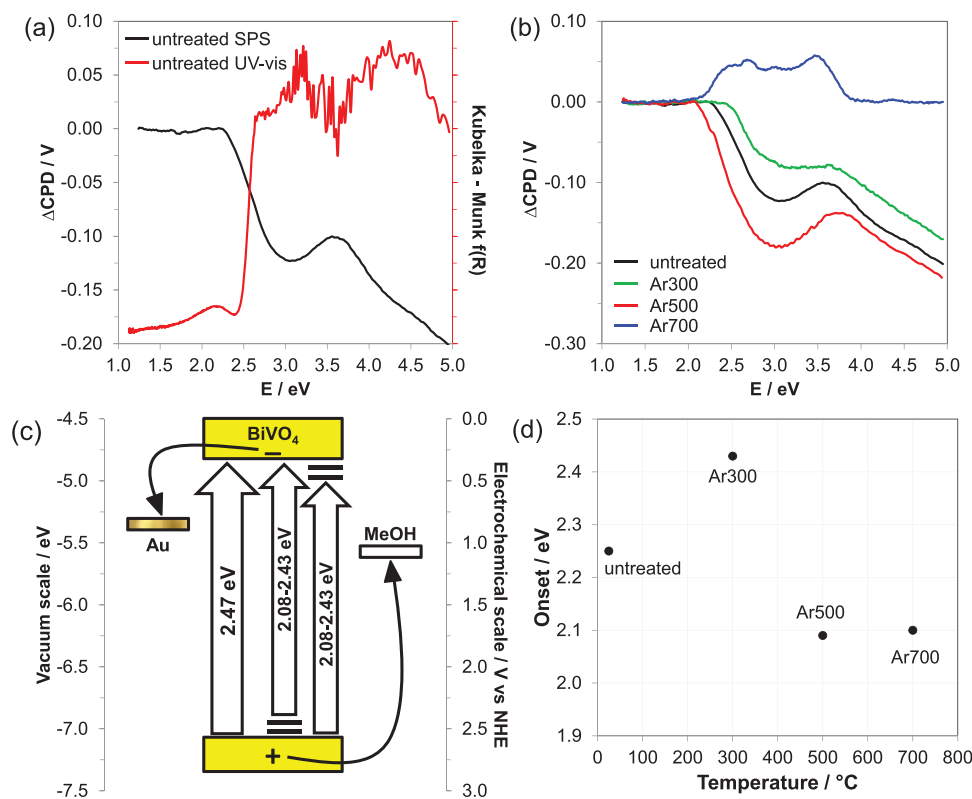


Figure 3. a) SPS spectrum for the untreated BiVO_4 overlaid with its UV-vis absorption spectrum. b) SPS spectra for all the samples. c) Energy diagram showing charge separation in the BiVO_4/Au system. The position of the sub gap states is tentative. d) A graph showing variation of the SPS onsets with annealing temperature.

electrons injecting into the Au can produce a maximum photovoltage of $[-5.3 \text{ eV} - (-4.76 \text{ eV})]/e = -0.54 \text{ V}$. The lower experimental value of -0.12 V is ascribed to low electron mobility in the BiVO_4 particulate film, which restricts charge separation in BiVO_4 particles in direct contact with the Au substrate. This is confirmed by the absence of stronger photovoltage signals in thicker films (data not shown). The SPS spectrum in Figure 3a further shows that the photovoltage does not revert to zero at the end of the scan. This means that the charge separation is irreversible, likely to trapping of photogenerated holes near the particle surface or reaction with surface adsorbed methanol molecules.

Figure 3b shows the surface photovoltage spectra for the Ar-annealed samples (data in Table 2). The spectra for the Ar300 and Ar500 samples are similar to the untreated BiVO_4 . However, for Ar700, the photovoltage spectrum is inverted. Furthermore, changes are observed in the photoonset across the sample series, as shown in Figure 3d. These variations indicate

Table 2. The ΔCPD value at the local maximum and SPS photoonset for each film.

Sample	$\Delta\text{CPD} [\text{V}]$	Photoonset [V]
Untreated	-0.123	2.25
Ar300	-0.081	2.43
Ar500	-0.181	2.08
Ar700	+0.057	2.10

changes in the defect state concentration in the BiVO_4 particles. For example, the Ar500 and Ar700 samples have photoonsets at 2.08 and 2.10 eV, $\approx 0.3 \text{ eV}$ below their optical bandgaps (Table 2), whereas the photoonsets for the untreated BiVO_4 and Ar300 are at 2.25 and 2.43 eV. This shows that thermal annealing modifies the electronic structure of the BiVO_4 particles. Annealing at $300 \text{ }^{\circ}\text{C}$ removes defects in Ar300, as supported by the slight increase of its crystallinity based on the XRD results, and pushes the photoonset closer to the optical bandgap of the material. Annealing at $500 \text{ }^{\circ}\text{C}$ or higher produces new subgap states near the conduction or valence band edge, which are responsible for the earlier onset in Ar500 and Ar700. In Ar500, these subgap states also improve charge transport through the BiVO_4 film, allowing for a photovoltage of -0.181 V (the largest in the sample series). However, in Ar700, the subgap states cause trapping of electrons and reversal of the charge transfer direction. Overall, the SPS results show that argon annealing induces changes in charge transport and trapping across the BiVO_4 series, depending on the temperature.

X-ray photoelectron spectroscopy (XPS) analysis was utilized to determine the change in surface chemical states of the Ar-treated BiVO_4 samples. Figure 4a-c shows the core levels of V 2p, O 1s, and Bi 4f XPS spectra of the samples. The V 2p XPS spectra (Figure 4a) of all samples exhibit V 2p_{3/2} and V 2p_{1/2} peaks at 516.9 and 524.6 eV, respectively, that are consistent with the values reported for BiVO_4 .^[7c] Each of the V 2p_{3/2} peak can be deconvoluted into two components V⁵⁺ and V⁴⁺ with the latter appearing at lower binding energy.

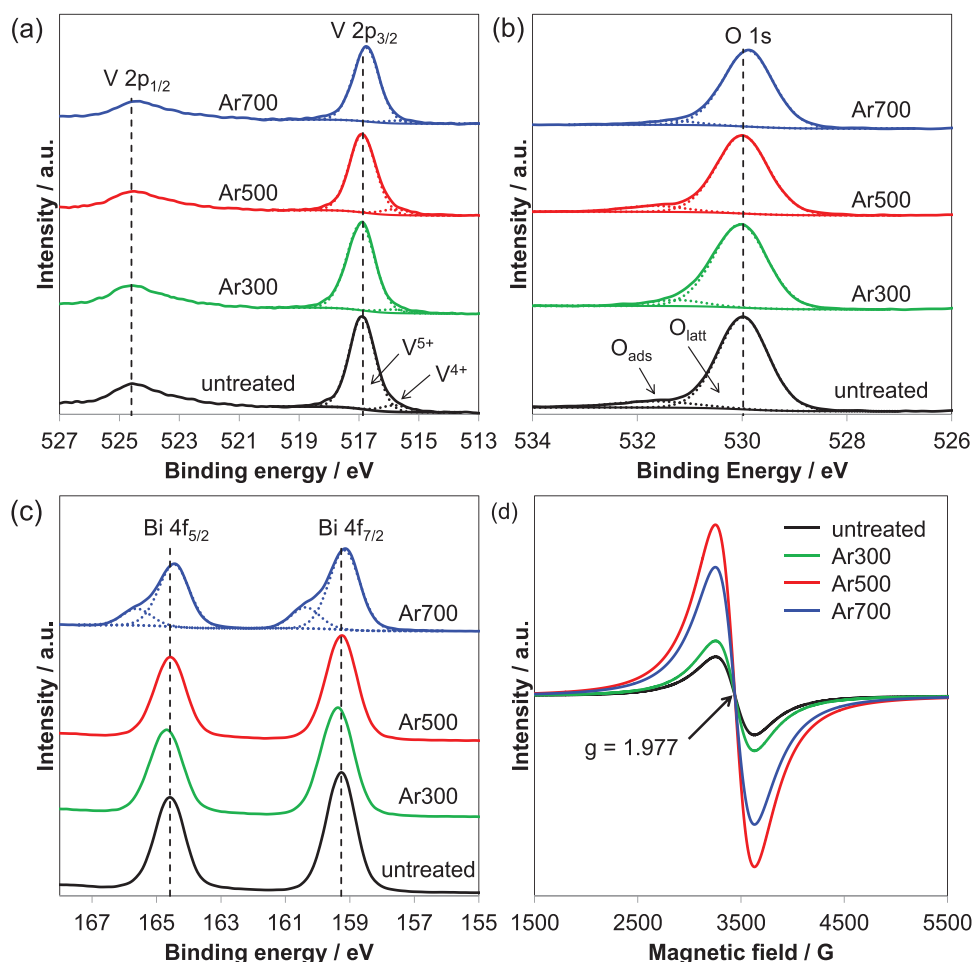


Figure 4. High-resolution XPS spectra of the a) V 2p, b) O 1s, and c) Bi 4f core levels of the BiVO_4 samples before and after Ar annealing treatment at different temperatures. d) The corresponding room temperature EPR spectra of all samples.

The asymmetric nature of O 1s signal (Figure 4b) indicates the presence of two oxygen species, namely, surface lattice oxygen (O_{latt}) and adsorbed oxygen (O_{ads}) with respective binding energies of 530.0 and 531.7 eV. Since both V^{4+} and O_{ads} are associated with oxygen vacancies,^[24] the presence of these two species confirms that oxygen vacancies exist on the surface of all samples. Despite SPS photoonset observations suggesting that new subgap states (likely to be oxygen vacancies) are present on Ar500 and Ar700, a corresponding increase of both the V^{4+} and O_{ads} species was not observed in the V 2p and O 1s XPS spectra of the two samples. This may be attributed to the minute variation of the oxygen vacancy density between the samples, which is beyond the sensitivity of XPS. As for the Bi 4f XPS spectra (Figure 4c), all samples display two distinct peaks located at around 159.3 and 164.6 eV which can be assigned to Bi $4f_{7/2}$ and Bi $4f_{5/2}$, respectively, corresponding to Bi^{3+} typically reported for BiVO_4 .^[25] Notably, an apparent broadening of these peaks with discernible shoulders at a higher binding energy is observed solely for Ar700. Deconvolution suggests that there are additional peaks at 160.4 and 165.6 eV, which are indicative of Bi centers with a higher oxidation state and can be attributed to surface bismuth vacancies.^[26] The result substantiates the presence of bismuth vacancies on the surface of Ar700.

It is known that the oxygen vacancy-related V^{4+} is paramagnetic. The relative density of oxygen vacancies of the BiVO_4 samples could be quantified by comparing their relative amount of V^{4+} using electron paramagnetic resonance (EPR) spectroscopy, which is highly sensitive for paramagnetic states even at extremely low concentrations.^[27] Figure 4d compares the room temperature EPR spectra of all samples, whereby a signal centered at $g = 1.977$ (corresponds to the g value reported for paramagnetic V^{4+})^[28] is observed for each sample. Importantly, while the EPR signal of Ar300 is comparable to that of the untreated BiVO_4 , the signal for Ar500 is markedly increased. These EPR results are in accordance with the SPS photoonset, inferring that the new subgap states for Ar500 arise from the formation of more oxygen vacancies. However, further increase of the annealing temperature to 700 °C diminishes the oxygen vacancy density, as indicated by the weaker EPR signal of Ar700 relative to that of Ar500. On the basis of the lower V^{4+} concentration but comparable SPS photoonset of Ar700 in comparison to Ar500, the subgap states of Ar700 are thus concluded to comprise both oxygen and bismuth vacancies, whereby the latter was validated by the Bi 4f XPS results discussed earlier.

The results of the above-mentioned spectroscopic characterization techniques verify that Ar annealing treatment improves

the crystallinity and affects the local structure distortion of BiVO_4 , which play a role in governing the photoactivity of BiVO_4 . Higher crystallinity signifies presence of less number of recombination sites to abate charge recombination, whereas greater orbital overlap allows better delocalization of photogenerated electrons and holes. These changes lead to more efficient charge separation which then explains the best activity exhibited by Ar500, in both the PS water oxidation reaction and the PEC photocurrent generation. The EPR results also revealed and confirmed that annealing treatment in the oxygen-deficient Ar atmosphere boosts oxygen vacancy formation in BiVO_4 , particularly at a temperature of 500 °C or higher. The considerable augmentation of oxygen vacancies in Ar500 is another factor contributing to its superior photoactivity. Oxygen vacancies have been predicted by the density functional theory (DFT) calculations as shallow donors in monoclinic BiVO_4 with low formation energies,^[12,29] which can increase the donor densities of the material for enhanced charge transport. These advantages of oxygen vacancies in BiVO_4 were demonstrated in numerous studies related to hydrogenation treatment,^[7c,12,30] whereby the H_2 -treated BiVO_4 showed better PEC water oxidation performance than that of the air-annealed sample.

Likewise, given that the crystallinity of Ar300 is only slightly improved compared to the untreated BiVO_4 and they both have comparable density of oxygen vacancies, it is reasonable to conclude that their photoactivities are comparable. Based on the most profound changes of structural, optical, and electronic properties exhibited by Ar700, a corresponding improvement in its photoactivity may be initially envisaged. However, the performance of Ar700 in the two activity tests executed was considerably poorer than that of the untreated BiVO_4 . This can be due to the creation of surface bismuth vacancies as corroborated by XPS analysis. Surface bismuth vacancy formation is possibly due to bismuth volatilization at high-temperature annealing, a phenomenon which has commonly been observed in the sintering process of bismuth-containing ceramic materials, contributing to the loss of bismuth element.^[31] This is especially significant at elevated temperatures. DFT calculations by Yin et al.^[29] and Wang et al.^[12] collectively suggest that bismuth vacancies are shallow acceptors in monoclinic BiVO_4 . The creation of surface bismuth vacancies thus encourages undesirable electron trapping on Ar700 (as supported by the positive SPS ΔCPD signal), confining the photogenerated electrons and impeding their reaction with Ag^+ ions, leading to poor O_2 generation. Similarly, the trapping phenomenon hampers electron transfer efficiencies of the Ar700 photoanode to result in low photocurrent generation by this sample.

Aside from the induced surface bismuth vacancies, the exceptionally poor photoactivity of Ar700 can also be ascribed to the well-defined crystal facets of the BiVO_4 diminishing under annealing treatment at high temperature. **Figure 5** presents the scanning electron microscopy (SEM) images of the Ar-treated samples along with the untreated BiVO_4 . The morphology of the Ar700 particles has evidently changed with regards to that of the other samples. As illustrated in Figure 5a, the untreated BiVO_4 particles are dual-faceted with exposed {010} and {110} facets, where the facet assignments are schematically depicted in the inset based on our previous work.^[16] While the

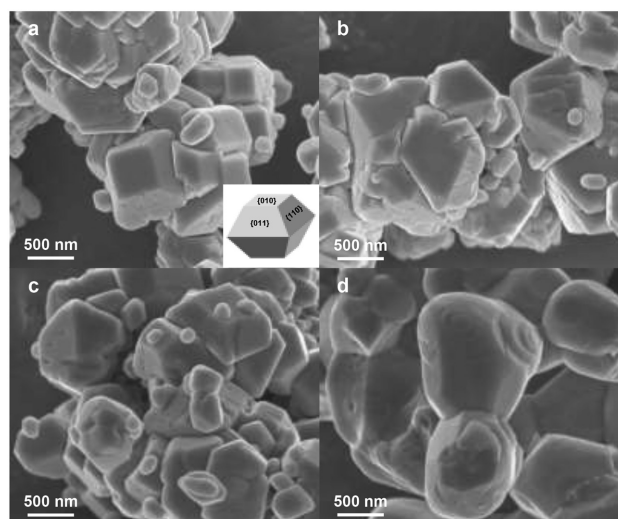


Figure 5. SEM images of the a) untreated BiVO_4 and Ar-treated BiVO_4 samples prepared at b) 300, c) 500, and d) 700 °C.

well-developed {010} and {110} facets are conserved in Ar300 and Ar500 (Figure 5b,c, respectively), they diminished in Ar700 (Figure 5d) whereby the particles become rounded with ridged surface.

{010} and {110} have been revealed as the redox functional facets of monoclinic BiVO_4 , in which photogenerated electrons and holes are spatially separated on the two surfaces.^[10] Therefore, the presence of well-developed {010} and {110} facets is essential for efficient charge separation. In order to validate the crystal facet-mediated charge separation, the BiVO_4 samples with and without the well-defined facets (represented by the untreated BiVO_4 and Ar700, respectively) were separately suspended in an aqueous solution containing platinum (Pt) salt and irradiated with visible light ($\lambda > 420$ nm). Reduction of the Pt salt by receiving photogenerated electrons from BiVO_4 forms metal Pt on the surface of the photocatalyst. This is generally known as the photoreduction process. After a 5 h illumination, the powder samples were collected and observed using a SEM microscope. The deposition of Pt metal is verified with the presence of small particles on the surface of the untreated BiVO_4 (Figure 6c) and Ar700 (Figure 6d), which surfaces are otherwise particle-free (Figure 6a,b, respectively) prior to their exposure to Pt salt under illumination. Note that the Pt particles are solely deposited on the {010} surface of the untreated BiVO_4 , suggesting that the photogenerated electrons are mainly available on the {010}, which is in perfect agreement with that observed by Li et al.^[10] Such discernible selectivity of Pt deposition on the {010} facet is clearly undermined in Ar700, where the Pt particles are randomly deposited on the surfaces with diminished {010} and {110} facets. The better selectivity of Pt deposition on the untreated BiVO_4 as opposed to Ar700 thus manifests better charge separation in BiVO_4 with well-developed {010} and {110} facets.

Apart from the single photodeposition of Pt metal, the role of {010} and {110} facets in facilitating charge separation was further substantiated by simultaneous photodeposition of Pt and manganese oxide (MnO_x). In the presence of both Pt and

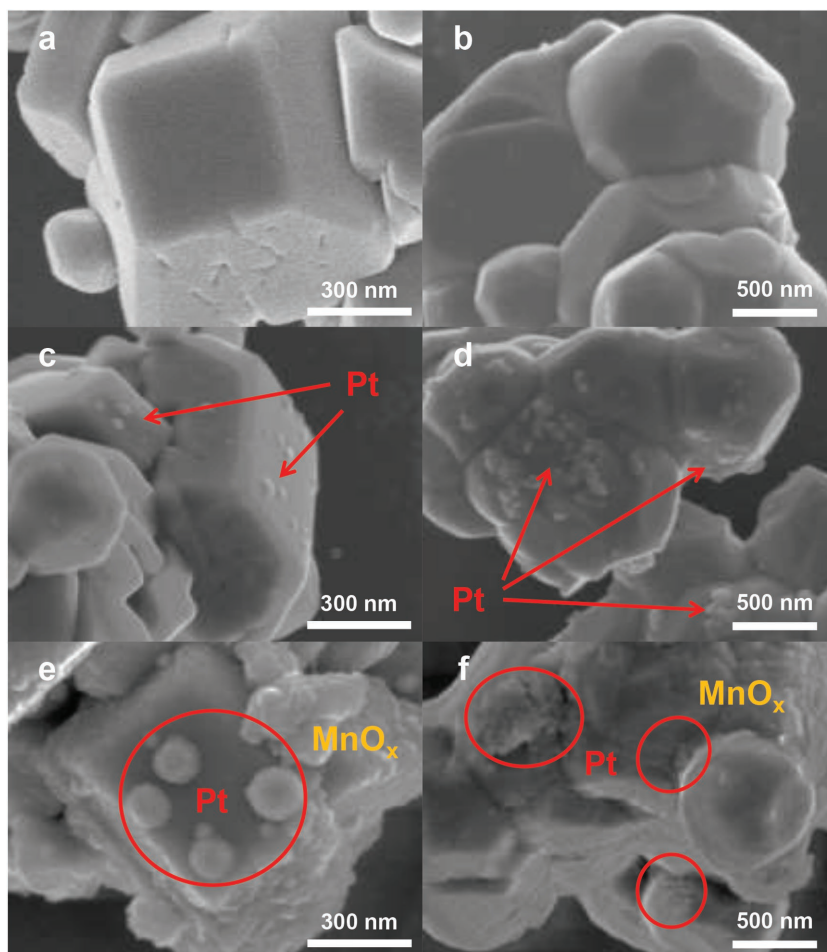


Figure 6. SEM images of the a) untreated BiVO_4 , b) Ar700, c) Pt-loaded untreated BiVO_4 , d) Pt-loaded Ar700, e) Pt/MnO_x -loaded untreated BiVO_4 , and f) Pt/MnO_x -loaded Ar700. (e) highlights facet-selective depositions of Pt and MnO_x on the untreated BiVO_4 with well-developed $\{010\}$ and $\{110\}$ facets.

manganese (Mn) salts, Li et al.^[10] have demonstrated that the latter can be oxidized to produce insoluble sponge-like MnO_x by accepting holes from the light-activated BiVO_4 when the electrons are involved in the reduction of the former to form Pt particles. Figure 6e,f displays the SEM images of Pt and MnO_x deposited on the untreated BiVO_4 and Ar700, respectively. The successful depositions of Pt and MnO_x on the untreated BiVO_4 (1.33 wt% Pt and 0.53 wt% Mn) and Ar700 (1.51 wt% Pt and 0.58 wt% Mn) were confirmed using inductively coupled plasma optical emission spectroscopy (ICP-OES) analysis, whereby loadings of Pt and Mn were found to be comparable between both samples. In the case of the untreated, well-faceted BiVO_4 , sponge-like MnO_x deposits are primarily formed on the $\{110\}$ facets, whereas the Pt particles are selectively deposited on the $\{010\}$ surfaces. The SEM image clearly shows that other than the deposition of Pt particles, the $\{010\}$ surface is completely free of the MnO_x deposits. This highly selective deposition of Pt on the $\{010\}$ facets and MnO_x on the $\{110\}$ facets marks good charge separation in BiVO_4 with well-developed facets, whereby photogenerated electrons and holes are preferentially driven to the $\{010\}$ and $\{110\}$ surfaces, respectively. On

the other hand, the surfaces of Ar700 particles with diminished $\{010\}$ and $\{110\}$ facets are fully covered by sponge-like MnO_x with patches of Pt agglomerates noticeable, indicating the lack of charge separation in this sample.

3. Conclusions

Ar annealing was demonstrated to affect the activity of dual-faceted BiVO_4 for photocatalytic O_2 generation and PEC photocurrent generation, attributing to the variation in physicochemical and electronic properties of the material. XRD, Raman, UV-vis, SPS, and EPR spectroscopic characterizations revealed that not only did Ar annealing enhance the crystallinity, local structure distortion, and optical properties of BiVO_4 , but also introduces new subgap states attributed to oxygen vacancies. Higher annealing temperature induces better crystallinity, greater orbital overlap, and smaller bandgap as well as favors oxygen vacancy formation, while improving charge separation, transport, and photoactivity of BiVO_4 . Despite Ar700 having the most significant changes on the aforesaid properties, Ar500 displayed the best activity in both the PS and PEC systems. This is due to the introduction of additional surface bismuth vacancies and diminution of well-developed facets upon annealing at a high temperature of 700°C , subsequently resulting in the deterioration of photochemical charge separation and photoactivity of the BiVO_4 . These findings thus provide better understanding

on the utilization of Ar annealing as a facile route to affect charge separation and transport efficiencies of faceted BiVO_4 for its practical use in water splitting.

4. Experimental Section

Synthesis of BiVO_4 : Dual-faceted BiVO_4 particles were prepared using the same method reported in recent papers^[11,16] with an aqueous nitric acid (HNO_3) solution of 1.00 M. For annealing treatment, the BiVO_4 powder was heated at different temperatures (300 , 500 , and 700°C) for 2 h in a tube furnace equipped with continuous flow of Ar gas. Subsequently, the sample was allowed to cool under Ar flow.

Photocatalytic Irradiations: Photocatalytic oxygen evolution was performed in a closed gas circulation system.^[18b] 300 mg of BiVO_4 powder was dispersed in 150 mL of aqueous 0.05 M AgNO_3 solution (pH 4.5) in a top-irradiation cell with a Pyrex window. Prior to irradiation, the suspension was evacuated to ≈ 2 kPa and refilled with Ar. This process was repeated at least five times to remove dissolved gases. The oxygen gas evolved during light illumination was analyzed by an online gas chromatograph (Shimadzu GC-8A, TCD, Ar carrier gas). The facet-selective photodepositions of Pt/MnO_x were done via two approaches: (a) single reduction of PtCl_6^{2-} and (b) simultaneous reduction of

PtCl₆²⁻ and oxidation of Mn²⁺. In case (a), 100 mg of BiVO₄ powder was dispersed in 100 mL of aqueous solution containing predetermined amount of chloroplatinic acid (H₂PtCl₆; 2 wt% Pt with respect to BiVO₄). The suspension was irradiated for 5 h under continuous stirring and deaeration using Ar gas. The product was retrieved by suction filtration, washed with distilled water, and dried at 60 °C. Same steps were repeated for case (b) by using an aqueous solution containing both H₂PtCl₆ and manganese (II) nitrate tetrahydrate (Mn(NO₃)₂·4H₂O) with calculated amounts of 2 wt% Pt and 0.5 wt% Mn with respect to BiVO₄. Loadings of Pt and Mn were thereafter determined using ICP-OES analysis, whereby the sample was digested using aqua regia. A 300 W Xe lamp (Oriol) coupled with a 420 nm cutoff filter was used as the light source for the reactions described above. The light intensity at the flask was 389 mW cm⁻².

Photoelectrochemical Measurements: The BiVO₄ powder samples were first made into thin-film electrodes by dropcast method. An electrode was prepared by depositing 6 mL of 1 mg cm⁻³ BiVO₄/ethanol suspension onto 2 cm × 1.5 cm area of FTO conducting substrate. Thereafter, the electrodes were heated in an oven at 150 °C for 2 h. Photoelectrochemical measurements were carried out using an Autolab potentiostat (model PGSTAT302N) with a standard three-electrode cell, in which the BiVO₄ electrode, a platinum foil, and a saturated Ag/AgCl electrode were used as the working, counter, and reference electrodes, respectively. An aqueous 0.1 M sodium sulfate (Na₂SO₄, pH 6) solution saturated with N₂ was utilized as the electrolyte. The measurements were done via backside illumination of the BiVO₄ working electrode (from the FTO side) under chopped irradiation at a constant applied potential of 0 V versus Ag/AgCl. A 300 W Xe lamp (Oriol) installed a 420 nm cutoff filter was employed as the light source.

Materials Characterization: XRD analysis was performed using a Phillips Xpert Multipurpose X-ray Diffraction System operating at 45 kV and 40 mA using Cu Kα radiation (λ = 1.54 Å). The crystallite size was estimated from the Scherrer equation using the full width at half-maximum height of the peak at 2θ = 30.6°. Raman spectra were collected on Renishaw inVia Raman microscope with 514 nm argon ion laser. Diffuse reflectance spectra were recorded using Shimadzu UV-3600 UV-vis-NIR spectrophotometer and converted to absorbance using the Kubelka-Munk method. SEM images were obtained on a FEI Nova NanoSEM 450 FE-SEM microscope with an operating voltage at 5 kV. XPS was carried out using a Thermo Scientific ESCALAB250Xi probe with monochromated Al Kα radiation (hν = 1486.68 eV). The binding energy was calibrated using the C 1s peak at 284.8 eV as reference. EPR measurements were carried out on Bruker EMX-plus operating in the X-band (9.52 GHz) with a microwave power of 2 mW.

Surface Photovoltage Spectroscopy: The BiVO₄ powder samples were first dropcast onto Au substrates to make films. Au substrates were cleaned by sonicating in ethanol, then hydrogen peroxide and potassium hydroxide, and then water for 10 min each. BiVO₄ suspensions with concentrations of 5 mg BiVO₄/1 mL water were sonicated for 15 min and then 0.05 mL of a suspension was dropcast onto the Au substrate covering a 0.5 cm × 0.5 cm square (the area was controlled with polymer tape). Films were left to dry at room temperature before being heated in an oven at 60 °C for 1 h. Before SPS was performed on the films, each film was treated with a drop of methanol and left to dry at room temperature. All SPS measurements were performed using a gold mesh Kelvin probe (3 mm diameter, Delta PHI Besocke) as the reference mounted inside a home-built vacuum chamber (10⁻⁴ mbar) by a Pfeiffer HiCube 80 Eco turbo pump station. A sample placed in the chamber was illuminated with monochromatic light from a 150 W Xe lamp filtered through an Oriol Cornerstone 130 monochromator (1–10 mW cm⁻²). The measured CPD spectra were corrected for signal drift due to variations in vacuum conditions during the measurements by subtracting a drift background from the raw data. This resulted in the reported CPD values being referenced against the dark CPD voltage. All SPS measurements were taken under vacuum with a scan range of 1–5 eV.

Acknowledgements

The authors thank the Australian Research Council for financial support. The authors acknowledge the UNSW Mark Wainwright Analytical Centre for providing access to all the analytical instruments. F.E.O. acknowledges support by the U.S. Department of Energy, Office of Science, Office of Basic Energy Sciences under Award No. DE-SC-0001234.

Received: September 30, 2016

Revised: November 1, 2016

Published online:

- [1] a) B. M. Reddy, A. Khan, Y. Yamada, T. Kobayashi, S. Loidant, J.-C. Volta, *J. Phys. Chem. B* **2003**, *107*, 11475; b) H. S. Kang, J. S. Kang, J. W. Kim, S. Y. Lee, *J. Appl. Phys.* **2004**, *95*, 1246; c) J. Yu, B. Wang, *Appl. Catal., B* **2010**, *94*, 295.
- [2] a) A. K. Bhattacharya, K. K. Mallick, A. Hartridge, *Mater. Lett.* **1997**, *30*, 7; b) D. Hanaor, C. Sorrell, *J. Mater. Sci.* **2011**, *46*, 855; c) J.-G. Yu, H.-G. Yu, B. Cheng, X.-J. Zhao, J. C. Yu, W.-K. Ho, *J. Phys. Chem. B* **2003**, *107*, 13871.
- [3] C. Ng, Y. H. Ng, A. Iwase, R. Amal, *ACS Appl. Mater. Interfaces* **2013**, *5*, 5269.
- [4] a) R. S. Hyam, J. Lee, E. Cho, J. Kim, H. Lee, *J. Nanosci. Nanotechnol.* **2012**, *12*, 8908; b) W. Mtangi, F. D. Auret, W. Meyer, M. Legodi, P. J. van Rensburg, S. Coelho, M. Diale, J. Nel, *J. Appl. Phys.* **2012**, *111*, 094504.
- [5] K. Yamada, H. Yamane, S. Matsushima, H. Nakamura, K. Ohira, M. Kouya, K. Kumada, *Thin Solid Films* **2008**, *516*, 7482.
- [6] G. Wang, Y. Ling, Y. Li, *Nanoscale* **2012**, *4*, 6682.
- [7] a) Y. Chae, S. Mori, M. Suzuki, *Thin Solid Films* **2009**, *517*, 4260; b) T. W. Kim, Y. Ping, G. A. Gallii, K.-S. Choi, *Nat. Commun.* **2015**, *6*, 8769; c) A. P. Singh, N. Kodan, A. Dey, S. Krishnamurthy, B. R. Mehta, *Int. J. Hydrogen Energy* **2015**, *40*, 4311.
- [8] G. Wang, H. Wang, Y. Ling, Y. Tang, X. Yang, R. C. Fitzmorris, C. Wang, J. Z. Zhang, Y. Li, *Nano Lett.* **2011**, *11*, 3026.
- [9] a) A. Kudo, K. Omori, H. Kato, *J. Am. Chem. Soc.* **1999**, *121*, 11459; b) A. Iwase, Y. H. Ng, Y. Ishiguro, A. Kudo, R. Amal, *J. Am. Chem. Soc.* **2011**, *133*, 11054.
- [10] R. Li, F. Zhang, D. Wang, J. Yang, M. Li, J. Zhu, X. Zhou, H. Han, C. Li, *Nat. Commun.* **2013**, *4*, 1432.
- [11] H. L. Tan, X. Wen, R. Amal, Y. H. Ng, *J. Phys. Chem. Lett.* **2016**, *7*, 1400.
- [12] G. Wang, Y. Ling, X. Lu, F. Qian, Y. Tong, J. Z. Zhang, V. Lordi, C. R. Leao, Y. Li, *J. Phys. Chem. C* **2013**, *117*, 10957.
- [13] Y. Liang, T. Tsubota, L. P. Mooij, R. van de Krol, *J. Phys. Chem. C* **2011**, *115*, 17594.
- [14] a) K. Maeda, *ACS Catal.* **2014**, *4*, 1632; b) J. Chang, W. Lin, M.-H. Hon, *Appl. Surf. Sci.* **2001**, *183*, 18; c) P. Nunes, B. Fernandes, E. Fortunato, P. Vilarinho, R. Martins, *Thin Solid Films* **1999**, *337*, 176.
- [15] M. Gotić, S. Musić, M. Ivanda, M. Šoufek, S. Popović, *J. Mol. Struct.* **2005**, *744*, 535.
- [16] H. L. Tan, H. A. Tahini, X. Wen, R. J. Wong, X. Tan, A. Iwase, A. Kudo, R. Amal, S. C. Smith, Y. H. Ng, *Small* **2016**, *12*, 5295.
- [17] J. Liu, H. Wang, S. Wang, H. Yan, *Mater. Sci. Eng., B* **2003**, *104*, 36.
- [18] a) J. Yu, A. Kudo, *Adv. Funct. Mater.* **2006**, *16*, 2163; b) Y. K. Kho, W. Y. Teoh, A. Iwase, L. Mädler, A. Kudo, R. Amal, *ACS Appl. Mater. Interfaces* **2011**, *3*, 1997.
- [19] a) I. t. Brown, K. K. Wu, *Acta Crystallogr., Sect. B* **1976**, *32*, 1957; b) F. D. Hardcastle, I. E. Wachs, *J. Phys. Chem.* **1991**, *95*, 5031.
- [20] a) M. R. Waller, T. K. Townsend, J. Zhao, E. M. Sabio, R. L. Chamousis, N. D. Browning, F. E. Osterloh, *Chem. Mater.*

- 2012, 24, 698; b) F. E. Osterloh, M. A. Holmes, L. Chang, A. J. Moulé, J. Zhao, *J. Phys. Chem. C* **2013**, 117, 26905.
- [21] a) R. Beranek, B. Neumann, S. Sakthivel, M. Janczarek, T. Dittrich, H. Tributsch, H. Kisch, *Chem. Phys.* **2007**, 339, 11; b) J. Zhao, F. E. Osterloh, *J. Phys. Chem. Lett.* **2014**, 5, 782.
- [22] Y. Yang, J. Wang, J. Zhao, B. A. Nail, X. Yuan, Y. Guo, F. E. Osterloh, *ACS Appl. Mater. Interfaces* **2015**, 7, 5959.
- [23] J. Wang, F. E. Osterloh, *J. Mater. Chem. A* **2014**, 2, 9405.
- [24] a) H. Jiang, H. Dai, X. Meng, K. Ji, L. Zhang, J. Deng, *Appl. Catal., B* **2011**, 105, 326; b) Y. Liu, H. Dai, J. Deng, L. Zhang, C. T. Au, *Nanoscale* **2012**, 4, 2317.
- [25] a) Y. Zhang, Y. Guo, H. Duan, H. Li, C. Sun, H. Liu, *Phys. Chem. Chem. Phys.* **2014**, 16, 24519; b) J. Su, X.-X. Zou, G.-D. Li, X. Wei, C. Yan, Y.-N. Wang, J. Zhao, L.-J. Zhou, J.-S. Chen, *J. Phys. Chem. C* **2011**, 115, 8064.
- [26] L. Zhang, W. Wang, D. Jiang, E. Gao, S. Sun, *Nano Res.* **2015**, 8, 821.
- [27] M. Che, J. C. Védrine, *Characterization of Solid Materials and Heterogeneous Catalysts: From Structure to Surface Reactivity*, Wiley, Weinheim, Germany, **2012**.
- [28] S. Gupta, N. Khanijo, A. Mansingh, *J. Non-Cryst. Solids* **1995**, 181, 58.
- [29] W.-J. Yin, S.-H. Wei, M. M. Al-Jassim, J. Turner, Y. Yan, *Phys. Rev. B* **2011**, 83, 155102.
- [30] a) J. Gan, X. Lu, B. B. Rajeeva, R. Menz, Y. Tong, Y. Zheng, *ChemElectroChem* **2015**, 2, 1385; b) Y. Zhang, D. Wang, X. Zhang, Y. Chen, L. Kong, P. Chen, Y. Wang, C. Wang, L. Wang, Y. Liu, *Electrochim. Acta* **2016**, 195, 51.
- [31] J. König, M. Spreitzer, B. Jančar, D. Suvorov, Z. Samardžija, A. Popovič, *J. Eur. Ceram. Soc.* **2009**, 29, 1695.